

# Tunable optical properties of multilayers black phosphorus

Tony Low,<sup>1,2,\*</sup> A. S. Rodin,<sup>3</sup> A. Carvalho,<sup>4</sup> Yongjin Jiang,<sup>5</sup> Han Wang,<sup>1</sup> Fengnian Xia,<sup>2</sup> and A. H. Castro Neto<sup>3,4</sup>

<sup>1</sup>IBM T.J. Watson Research Center, 1101 Kitchawan Rd., Yorktown Heights, NY 10598, USA

<sup>2</sup>Department of Electrical Engineering, Yale University, New Haven, Connecticut 06511

<sup>3</sup>Boston University, 590 Commonwealth Ave., Boston, MA 02215, USA

<sup>4</sup>Graphene Research Centre & Department of Physics,  
National University of Singapore, 117542, Singapore

<sup>5</sup>Zhejiang Normal University, Jinhua 321004, Peoples Republic of China

(Dated: January 20, 2022)

We calculated the optical conductivity tensor of multilayers black phosphorus using the Kubo formula within an effective low-energy Hamiltonian. The optical absorption spectra of multilayers black phosphorus are shown to vary sensitively with thickness, doping, and light polarization. In conjunction with experimental spectra obtained from infrared absorption spectroscopy, we discuss the role of interband coupling and disorder on the observed anisotropic absorption spectra. Multilayers black phosphorus might offer attractive alternatives to narrow gap compound semiconductors for optoelectronics across mid- to near-infrared frequencies.

**Introduction**— The group V element phosphorus can exist in several allotropes, and one of its thermodynamically more stable phase under room temperature and pressure condition is black phosphorus (BP). Similar to graphene, it is also a layered material, except that each layer forms a puckered surface due to  $sp^3$  hybridization. The electrical, optical and structural properties of single crystalline and polycrystalline BP had been extensively studied in the past[1–5]. Bulk BP is a semiconductor with a direct band gap of about 0.3 eV. Measured Hall mobilities in  $n$  and  $p$ -type samples almost approach  $10^5$  cm<sup>2</sup>/Vs. In addition, its electrical and optical properties are also highly sensitive to crystallographic orientation. Very recently, BP was re-introduced[6–9] in their multilayers thin film form, obtained from the simple mechanical exfoliation[10]. Preliminary electrical data on multilayers BP field-effect transistors showed encouraging results.

In this work, we examine the optical properties of multilayers BP with thickness ranging from few to tens of nanometers. We calculate its optical conductivities using the Kubo formula, within the framework of an effective low-energy Hamiltonian[11]. Our calculations show that the optical absorption spectra of multilayers BP vary sensitively with thickness, doping and light polarization, especially across the technologically relevant mid- to near-infrared spectrum. In conjunction with experimental spectra obtained from Fourier transform infrared spectroscopy (FTIR)[8], we elucidate the role of interband coupling and disorder on the observed anisotropic absorption spectra.

**Model**— BP has an orthorhombic crystal structure consisting of puckered layers as illustrated in Fig. 1. Lattice constant in the out-of-plane direction is about 10.7 Å, where effective layer-to-layer distance is half of this. In multilayers BP, translational symmetry in the  $z$ -direction is broken, and its bandstructure has a direct energy gap at the  $\Gamma$  point instead of the  $Z$  point in bulk. In order to

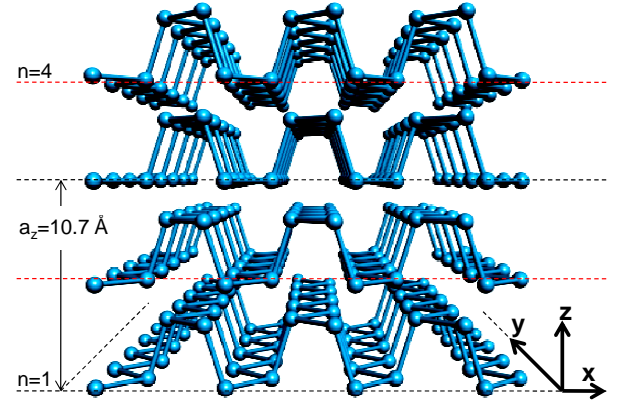


FIG. 1: Lattice structure of black phosphorus(BP). Layer numbers  $n$  is indicated.  $a_z$  is the lattice constant in the out-of-plane direction. Thickness of the multilayers BP is then given by  $t_z = n * a_z/2$ . Crystallographic axes  $\{xyz\}$  used in this work are defined.

describe the system behavior around the  $\Gamma$  point, we use first principles calculations in conjunction with the  $\mathbf{k}\cdot\mathbf{p}$  approximation[11].

Before constructing the low-energy Hamiltonian, we analyze the system symmetry. Individual monolayers, due to puckering, have a reduced symmetry compared to graphene, represented by the  $C_{2h}$  point group. The principal axis, which we denote  $\hat{y}$ , runs along the buckles. The reflection plane  $\sigma_h$  lies in the  $x$ - $z$  plane. It is possible to show that at the  $\Gamma$  point wavefunctions are either even or odd with respect to reflection across  $\sigma_h$ . From *ab initio* calculations, we determined that the highest valence and the lowest conduction bands are even and composed primarily of  $s$ ,  $p_x$ , and  $p_z$  orbitals with a small contribution from even  $d$  orbitals. Odd wavefunctions, made up of mostly  $p_y$ , are more energetically separated from the Fermi level. Keeping this in mind, we now proceed to construct an effective Hamiltonian that describes

the coupled valence and conduction bands.

In  $\mathbf{k}\cdot\mathbf{p}$  approximation, the perturbing Hamiltonian is given by  $\mathcal{H}_1 = \hbar(k_x\hat{p}_x + k_y\hat{p}_y)/m_0$ . To determine the coupling between the bands, one needs to compute the matrix elements of  $\mathcal{H}_1$  for the two bands of interest. Since  $\hat{p}_x$  is even with respect to  $\sigma_h$  reflection, it gives a finite contribution to the matrix element. On the other hand, the fact that  $\hat{p}_y$  is odd prohibits the term linear in  $k_y$ . If one disregards the remaining bands, the system becomes quasi-one-dimensional close to the  $\Gamma$  point. To introduce  $k_y$  dependence, we utilize the Löwdin partitioning. The leading order correction to the effective Hamiltonian is given by

$$(\mathcal{H}_1^{(2)})_{mm'} = \sum_l \frac{(\mathcal{H}_1)_{ml}(\mathcal{H}_1)_{lm'}}{2} \left[ \frac{1}{E_m - E_l} + \frac{1}{E_{m'} - E_l} \right], \quad (1)$$

where the summation goes over the remaining bands. Because of the product of the matrix elements in the numerator, it is clear that the leading order  $k_y$  contribution to the coupling terms will be quadratic, arising from the mixing with the odd bands. This allows one to write down the low-energy in-plane Hamiltonian around the  $\Gamma$  point as[11],

$$\mathcal{H} = \begin{pmatrix} E_c + \eta_c k_x^2 + \nu_c k_y^2 & \gamma k_x + \beta k_y^2 \\ \gamma k_x + \beta k_y^2 & E_v - \eta_v k_x^2 - \nu_v k_y^2 \end{pmatrix} \quad (2)$$

where  $\eta_{c,v}$  and  $\nu_{c,v}$  are related to the effective masses, while  $\gamma$  and  $\beta$  describe the effective couplings between the conduction and valence bands.  $E_c$  and  $E_v$  are the conduction and valence band edge energies in bulk BP, where  $E_c - E_v$  is the bulk gap of  $\approx 0.3$  eV[4].

In multilayers BP, the confinement in the out-of-plane  $z$  direction leads to quantized subbands. The out-of-plane masses are taken to be  $m_{cz} \approx 0.2 m_0$  and  $m_{vz} \approx 0.4 m_0$ , obtained from cyclotron resonance measurement in bulk BP and bandstructure calculations[4, 12]. In-plane dispersion within each subband are described by Eq. 2, except that  $E_{c,v}$  are replaced with  $E'_{c,v}$ , where  $E'_c = E_c + j^2 \hbar^2 \pi^2 / 2m_{cz} t_z^2$ , where  $j$  labels the subband,  $t_z$  is the thickness of the BP film and  $m_{cz}$  is the electron effective mass along  $z$ . Analogous expressions apply also for the hole case. Close to the  $\Gamma$  point, the in-plane effective masses follow[11],

$$m_{cx}^j = \frac{\hbar^2}{2\gamma^2 / (E_c^j - E_v^j) + \eta_c}, \quad m_{cy}^j = \frac{\hbar^2}{2\nu_c} \quad (3)$$

The parameters  $\eta_{c,v}$ ,  $\nu_{c,v}$  and  $\gamma$  are chosen such that it yields the known effective masses in the bulk BP limit i.e.  $m_{cx} = m_{vx} = 0.08 m_0$ ,  $m_{cy} = 0.7 m_0$  and  $m_{vy} = 1.0 m_0$ [4, 12], and  $m_{cx} = m_{vx} \approx 0.15 m_0$  for monolayer BP[11] (with an estimated bandgap of  $\sim 2$  eV). We are less certain about the value of  $\beta$ , which was suggested to lie between  $1 - 10 a^2 / \pi^2$  eV m<sup>2</sup>[11], where  $a \approx 2.23$  Å and  $\pi/a$  is the width of the BZ in  $x$  direction. We tentatively

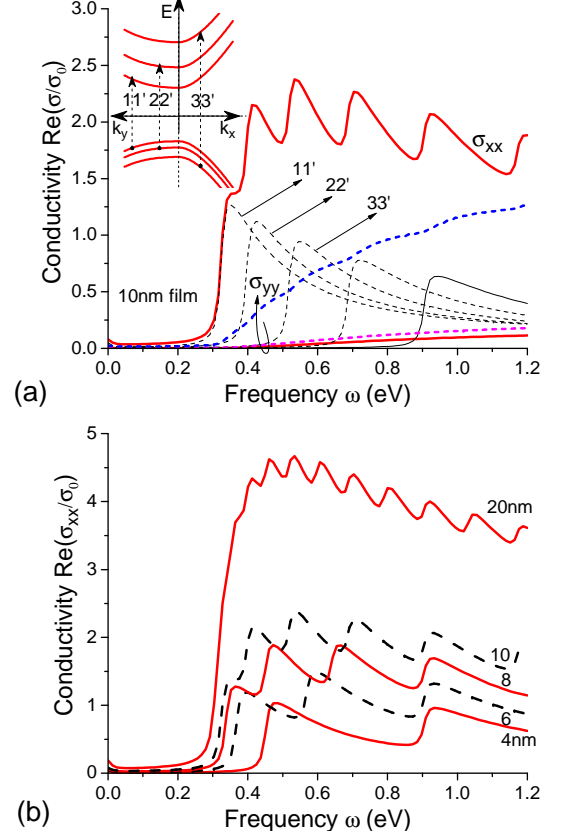


FIG. 2: (a) Real part of optical conductivities,  $\text{Re}(\sigma_{xx})$  and  $\text{Re}(\sigma_{yy})$ , for 10 nm thick intrinsic BP, i.e. Fermi level is located at mid-gap. See main text for parameters used in the calculations. Inter-subbands contributions to the  $\sigma_{xx}$  are plotted, where the respective optical transition processes are illustrated in inset.  $\sigma_{yy}$  calculated with  $2\times$  and  $10\times$  the value of  $\beta$  are also shown (dashed pink and blue lines respectively) for comparison. Conductivities are normalized with respect to  $\sigma_0 \equiv e^2/4\hbar$ . (b)  $\text{Re}(\sigma_{xx})$  for intrinsic BP of different thicknesses as indicated.

assign  $\beta \approx 2a^2/\pi^2$  eV m<sup>2</sup> and evaluate its effect on our calculated results in subsequent discussions below.

Physical quantities observed in optical experiments can often be expressed in terms of the optical conductivity. The Kubo formula for the conductivity tensor as function of frequency and momentum reads,

$$\sigma_{\alpha\beta}(\mathbf{q}, \omega) = -i \frac{g_s \hbar e^2}{(2\pi)^2} \sum_{ss'jj'} \int d\mathbf{k} \frac{f(E_{sj\mathbf{k}}) - f(E_{s'j'\mathbf{k}'})}{E_{sj\mathbf{k}} - E_{s'j'\mathbf{k}'}} \times \frac{\langle \Phi_{sj\mathbf{k}} | \hat{v}_\alpha | \Phi_{s'j'\mathbf{k}'} \rangle \langle \Phi_{s'j'\mathbf{k}'} | \hat{v}_\beta | \Phi_{sj\mathbf{k}} \rangle}{E_{sj\mathbf{k}} - E_{s'j'\mathbf{k}'} + \hbar\omega + i\eta} \quad (4)$$

where  $\hat{v}_\alpha$  is the velocity operator defined as  $\hbar^{-1} \partial_{k_\alpha} \mathcal{H}$ ,  $g_s = 2$  accounts for the spin degeneracy and  $\eta \approx 10$  meV accounts for the finite damping.  $f(\dots)$  is the Fermi-Dirac distribution function, where temperature is taken to be 300 K in all calculations. The indices  $\{s, s'\} = \pm 1$  denote

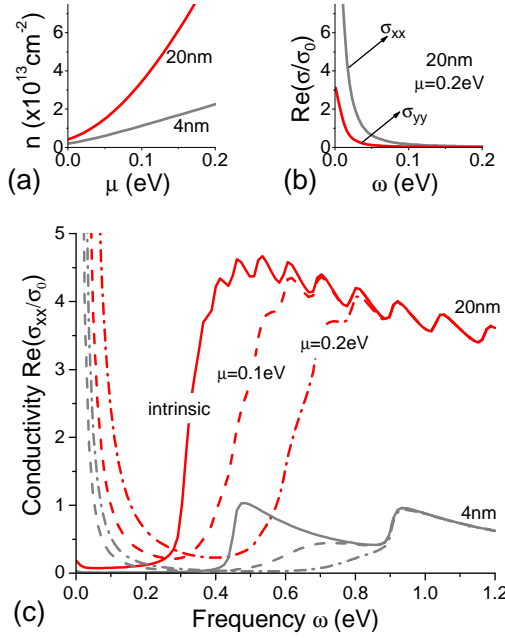


FIG. 3: (a) Electron densities ( $n$ ) as function of chemical potential ( $\mu$ ) for 20 nm and 4 nm BP films. (b) Optical conductivity  $\sigma_{xx}$  and  $\sigma_{yy}$  for 20 nm BP film doped at  $\mu = 0.2 \text{ eV}$ . (c)  $\text{Re}(\sigma_{xx})$  for BP with different chemical potential  $\mu$  as indicated, calculated for 4 nm and 20 nm thick films.

conduction/valence band, while  $\{j, j'\}$  are the subbands indices.  $E_{sj\mathbf{k}}$  and  $\Phi_{sj\mathbf{k}}$  are the eigen-energies and eigen-functions of  $\mathcal{H}$ . We have analytical expression for  $E_{sj\mathbf{k}}$ ;

$$E_{\pm j\mathbf{k}} = \frac{1}{2} [(E_c^j + E_v^j) + k_x^2(\eta_c - \eta_v) + k_y^2(\nu_c - \nu_v)] \pm \frac{1}{2} [\Delta^2 + \Delta (2k_x^2(\eta_c + \eta_v) + 2k_y^2(\nu_c + \nu_v)) + (k_x^2(\eta_c + \eta_v) + k_y^2(\nu_c + \nu_v))^2 + 4(\gamma k_x + \beta k_y^2)^2]^{1/2} \quad (5)$$

where  $\Delta \equiv E_c^j - E_v^j$ . Allowed optical transitions between these quantized subbands are when  $ss' = \pm 1$  (i.e. intra- and inter-band processes) and  $j = j'$ . Otherwise the matrix elements  $\langle \dots \rangle$  in Eq. 4 vanish. In this work, we are only interested in the local conductivity i.e.  $\sigma_{\alpha\beta}(\mathbf{q} \rightarrow 0, \omega)$ . In this limit, only the diagonal components of the conductivity tensor,  $\sigma_{xx}(\omega)$  and  $\sigma_{yy}(\omega)$ , are non-zero.

**Results**— Fig. 2a presents the calculated real part of optical conductivities of an undoped 10 nm BP thin film. Temperature is taken to be 300 K in all calculations. Results are normalized with respect to  $\sigma_0 = e^2/4\hbar$ , the well-known universal conductivity of graphene[13, 14]. The large asymmetry between  $\sigma_{xx}$  and  $\sigma_{yy}$  is immediately apparent. We note that this asymmetry has less to do with the in-plane effective mass anisotropy, as the qualitative trends persist even if we set  $m_x = m_y$  (not shown). Instead,  $\sigma_{yy}$  increases almost linearly with the interband coupling term,  $\beta$ , as shown (pink and blue dashed line). However, within the reasonable range of  $\beta$  values from  $1 - 10a^2/\pi^2 \text{ eV m}^2$ , the magnitude of  $\sigma_{xx}$  remains rela-

tively unchanged.

As shown in Fig. 2a,  $\sigma_{xx}$  exhibits an oscillatory behavior with  $\omega$  which can be traced to the underlying electronic subbands structure. Since it is undoped, only interband transitions from conduction to valence band are permitted. The zero wavefunction overlap between different subbands and a transition dipole moment normal to the light polarization, implies that only  $j = j'$  transitions are allowed, as illustrated in the inset. Fig. 2b shows the calculated  $\sigma_{xx}$  for BP films of different thicknesses  $t_z$  from 20 – 4 nm. The absorption edge moves from 0.3 eV to 0.6 eV with decreasing  $t_z$  due to the increasing energy gap. Maximal  $\sigma_{xx}$  also decreases as a result. Due to reduced screening for thinner films, strong excitonic effects is expected[15], which would lead to enhanced light absorption not account for in present calculations.

Doping can be induced either electrically[6–8] or chemically by introducing donor or acceptor impurity atoms during the synthesis[4]. Here, we consider the uniformly  $n$ -doped case. We defined the chemical potential  $\mu$  to be the difference between the Fermi level and the first conduction subband i.e.  $E_F - E_c^1$ . The electron density,  $n$ , follows from Fermi statistics and is given by,

$$n = \sum_j \frac{m_{dos}^j k_B T}{\pi \hbar^2} \log \left[ 1 + \exp \left( \frac{E_F - E_c^j}{k_B T} \right) \right] \quad (6)$$

where  $m_{dos}^j = (m_{cx}^j m_{cy}^j)^{1/2}$  is the density-of-states mass. Fig. 3a shows  $n$  as a function of  $\mu$  for 4 nm and 20 nm films, where  $\mu \lesssim 0.2 \text{ eV}$  covers the range of dopings  $\lesssim 5 \times 10^{13} \text{ cm}^{-2}$ . These dopings are routinely obtained in experiments with layered materials. Following the increased in doping will be the appearance of Drude absorption peak at  $\omega \rightarrow 0$ . Fig. 3b plots the optical conductivities,  $\sigma_{xx}$  and  $\sigma_{yy}$ , for a doped 20 nm BP film. The asymmetry here is due to the larger Drude weight  $\mathcal{D}$  for transport along  $x$ , to be discussed below.

Fig. 3c studies the optical property of multilayers BP with doping ranging from  $\mu = 0 - 0.2 \text{ eV}$ . Simple picture for direct optical transitions would suggest a blue-shift in the absorption edge by  $2\mu$  due to Pauli blocking. Consider first the result for 20 nm film. Although the blue-shift is evident, it appears to be less than  $2\mu$ . The absorption edge also becomes less abrupt with increased doping. These trends become more pronounced in the 4 nm case.

Light scattering across a conducting layer in between two dielectric media can be solved using the Fresnel equation. For normal incident light, the reflection amplitude is given by,

$$r = \frac{\epsilon_0 c (\sqrt{\epsilon_2} - \sqrt{\epsilon_1}) + \sigma_{xx} \cos^2 \alpha + \sigma_{yy} \sin^2 \alpha}{\epsilon_0 c (\sqrt{\epsilon_2} + \sqrt{\epsilon_1}) + \sigma_{xx} \cos^2 \alpha + \sigma_{yy} \sin^2 \alpha} \quad (7)$$

where  $\epsilon_0$  is the free-space permittivity,  $c$  the speed of light and  $\alpha$  is the light polarization angle. The reflection

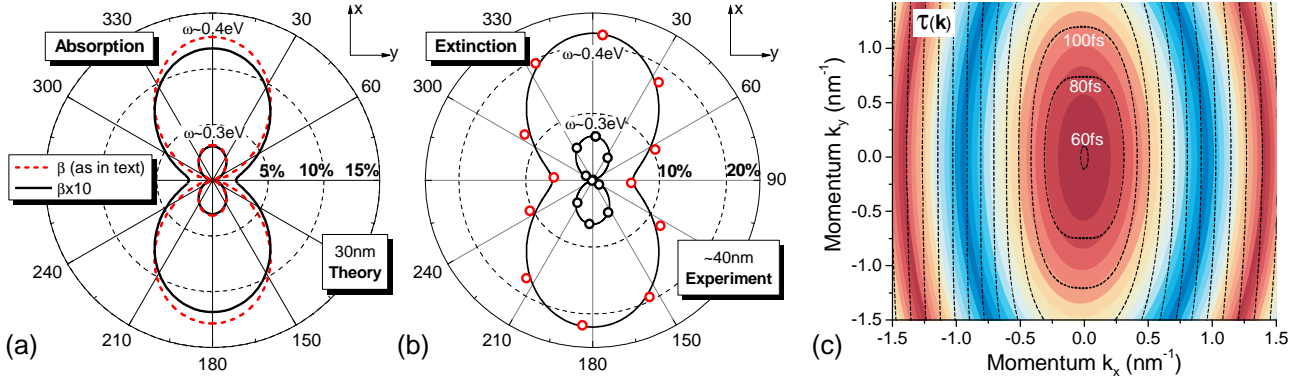


FIG. 4: (a) Polar representation of the absorption coefficient  $\mathcal{A}(\alpha)$  for a 30 nm intrinsic BP film for normal incident light with excitation energies larger than the band gap.  $\alpha$  is the light polarization angle.  $\mathcal{A}(\alpha)$  is plotted for two values of interband coupling strengths. (b) Polar representation of the experimental extinction spectra  $\mathcal{Z}(\omega)$  obtained from FTIR spectroscopy, for a  $\sim 40$  nm BP film on a  $\text{SiO}_2$  substrate[8]. We estimate that the beam spot size is  $\approx 2$  times larger than the sample size in experiment. Lines are fitted curves to the data using  $a\sin^2\theta + b\cos^2\theta$ . (c) Contour plots for single particle lifetime due to long-range Coulomb interaction, overlaid with the energy dispersion colour-filled contours. Each color step has an energy difference of 20 meV. See accompanying text for more descriptions on (b) and (c).

and transmission probabilities are given by  $\mathcal{R} = |r|^2$  and  $\mathcal{T} = |1 + r|^2 \sqrt{\epsilon_2/\epsilon_1}$ , and the absorption coefficient is  $\mathcal{A} = 1 - \mathcal{R} - \mathcal{T}$ .

Fig. 4a plots the angular dependent absorption coefficient,  $\mathcal{A}(\alpha)$ , for an intrinsic 30 nm BP film, with light excitations larger than the bandgap i.e. interband processes. We observed that  $\mathcal{A}(\alpha)$  exhibits strong dependence with polarization angle. The absorption anisotropy is rather sensitive to the interband coupling strength  $\beta$ , which evolves from a ‘dumbbell’-shape to a more elliptical form with increasing  $\beta$ . Disorder, as described by the phenomenological constant  $\eta$  in Eq. 4, has a milder effect (not shown).

FTIR spectroscopy is a common technique for obtaining infrared spectra of absorption. In Fig. 4b, we show the experimental extinction spectra  $\mathcal{Z}(\omega)$  for a 40 nm BP film on a  $\text{SiO}_2$  substrate. The extinction characterizes the differential transmission through the sample in regions with  $(\mathcal{T}(\omega))$  and without  $(\mathcal{T}_0(\omega))$  BP i.e.  $\mathcal{Z} = 1 - \mathcal{T}/\mathcal{T}_0$ . Experimental setup and details are elaborated elsewhere[8]. Note that  $\mathcal{Z}(\omega)$  includes both the additional light absorption and reflection due to the BP,  $\mathcal{Z}(\omega) > \mathcal{A}(\omega)$ . To account for the observed anisotropy in the experimental spectra, the model would entail an interband coupling strength of  $\beta \approx 20a^2/\pi^2 \text{ eV m}^2$  as depicted in Fig. 4a. This allows us to capture the main experimental features observed. It is very likely that extrinsic factors such as structural deformations, corrugations or defects also play a role in the conductivity anisotropy, which we defer to future studies.

On the contrary, intraband optical absorption in doped samples are primarily dictated by disorder. Due to the mass anisotropy, the Drude weight is different along the two crystallographic axes, and is given by  $\mathcal{D}_j = \pi n e^2 / m_j$  where  $j = \{x, y\}$ . In the zero and large frequencies limits,

the real part of Drude conductivity are given by  $\hbar \mathcal{D}_j / \pi \eta$  and  $\mathcal{D}_j \eta / \pi \hbar \omega^2$  respectively. Below, we discuss some common sources of disorders.

Impurities and defects are common source of disorder in 2D materials[16, 17]. For interactions of electrons with impurities, the self-energy within the Born approximation can be written as,

$$\Sigma(\mathbf{k}, E) = n_i \frac{g_s}{(2\pi)^2} \int d\mathbf{k}' \frac{|V(q)|^2 \mathcal{F}(\mathbf{k}, \mathbf{k}')}{E - E_{\mathbf{k}'} + i\eta_0} \quad (8)$$

where  $V(q)$  is the scattering potential,  $\mathcal{F}(\mathbf{k}, \mathbf{k}') \equiv |\langle \mathbf{k} | \mathbf{k}' \rangle|^2$  is the overlap function between states and  $\eta_0$  is taken to be 10 meV. For long-range Coulomb interaction, we have  $V(q) = e^2 \exp(-qd_0) / 2\epsilon_0 \kappa (q + q_s)$ , where  $\kappa$  is the effective dielectric constant taken to be 1 and  $d_0$  is an effective distance between BP and the impurities. Screening is treated within the Thomas-Fermi approximation with  $q_s = e^2 D / 2\pi \kappa$  being the screening wave-vector, and  $D$  is the 2D density-of-states. For short-range interaction, we simply have  $V(q) = V_0$ . Unlike the latter, long-range Coulomb interaction would lead to single particle damping that is angular dependent.

The single particle lifetime is given by  $\tau(\mathbf{k}) = \frac{\hbar}{2} \text{Im}[\Sigma(\mathbf{k}, E)^{-1}]$ , a quantity that can be directly measured using angle-resolved photoemission spectroscopy (ARPES). In Fig. 4c, we plot the contours for single particle lifetime due to long-range Coulomb interaction. For our estimates, we assume typical impurities concentration of  $n_i \approx 5 \times 10^{11} \text{ cm}^{-2}$  and  $d_0 \approx 1 \text{ nm}$ . The calculated lifetime contours,  $\tau(\mathbf{k})$ , is overlaid with the energy dispersion contours, and they are qualitatively different. This implies that electron interaction with long-range Coulomb impurities will lead to an anisotropic lifetime in general, and subsequently influencing also the conductivity anisotropy. In similar fashion, interaction with

acoustic phonons would also yield an anisotropic single particle lifetime due to the different sound velocities and deformation potentials along the two crystal axes.

*Conclusions*— In summary, we have presented a model for describing the optical properties in multilayers BP. Our results show that the optical conductivity, similarly the absorption spectra, of multilayers BP vary sensitively with thickness, doping and light polarization. The tunability is particularly effective for frequencies ranging from  $2500 - 5000 \text{ cm}^{-1}$ , which resides in the technologically relevant mid- to near-infrared spectrum. Hence, multilayers BP might offer attractive alternatives, in terms of tunability, flexibility and cost, to narrow gap compound semiconductors for infrared optoelectronics. We anticipate more upcoming experiments on the properties of multilayers BP, such as FTIR and ARPES, which can help shed light on the results presented here.

*Acknowledgements*— T.L. is grateful for the hospitality of Graphene Research Center, Singapore, where this work was initiated and conducted in large part. A.S.R. acknowledges DOE grant DE-FG02-08ER46512, ONR grant MURI N00014-09-1-1063. A.H.C.N. acknowledges NRF-CRP award “Novel 2D materials with tailored properties: beyond graphene” (R-144-000-295-281). The first-principles calculations were carried out on the GRC high-performance computing facilities.

*Supplemental Information*— Details of *ab initio* studies with extracted mass tensors are summarized.

---

\* Electronic address: tonyaslow@gmail.com

[1] R. W. Keyes, Physical Review **92**, 580 (1953).

- [2] D. Warschauer, Journal of Applied Physics **34**, 1853 (1963).
- [3] J. C. Jamieson, Science **139**, 1291 (1963).
- [4] A. Morita, Applied Physics A **39**, 227 (1986).
- [5] K. J. Chang and M. L. Cohen, Physical Review B: Condensed Matter **33**, 6177 (1986).
- [6] L. Li, Y. Yu, G. J. Ye, Q. Ge, X. Ou, H. Wu, D. Feng, X. H. Chen, and Y. Zhang, Nature Nanotechnology (2014).
- [7] H. Liu, A. T. Neal, Z. Zhu, D. Tomanek, and P. D. Ye, arXiv:1401.4133 (2014).
- [8] F. Xia, H. Wang, and Y. Jia, arXiv:1402.0270 (2014).
- [9] S. P. Koenig, R. A. Doganov, H. Schmidt, A. H. Neto, and B. Oezylmaz, Appl. Phys. Lett. **104**, 103106 (2014).
- [10] K. S. Novoselov, D. Jiang, F. Schedin, T. J. Booth, V. V. Khotkevich, S. V. Morozov, and A. K. Geim, Proceedings of the National Academy of Sciences of the United States of America **102**, 10451 (2005).
- [11] A. S. Rodin, A. Carvalho, and A. H. Neto, arXiv:1401.1801 (2014).
- [12] S.-i. Narita, S.-i. Terada, S. Mori, K. Muro, Y. Akahama, and S. Endo., Journal of the Physical Society of Japan **52**, 3544 (1983).
- [13] R. R. Nair, P. Blake, A. N. Grigorenko, K. S. Novoselov, T. J. Booth, T. Stauber, N. M. R. Peres, and A. K. Geim., Science **320**, 1308 (2008).
- [14] K. F. Mak, M. Y. Sfeir, Y. Wu, C. H. Lui, J. A. Misewich, and T. F. Heinz, Physical Review Letters **101**, 196405 (2008).
- [15] D. Y. Qiu, H. Felipe, and S. G. Louie, Physical Review Letters **111**, 216805 (2013).
- [16] A. C. Neto, F. Guinea, N. M. R. Peres, K. S. Novoselov, and A. K. Geim., Review of Modern Physics **81**, 109 (2009).
- [17] S. D. Sarma, S. Adam, E. H. Hwang, and E. Rossi, Review of Modern Physics **83**, 407 (2011).